AGU PUBLICATIONS

Geophysical Research Letters

RESEARCH LETTER
10.1002/2014GL061507

Key Points:
- Numerical modeling of normal fault evolution coupled with surface processes
- Surface processes sustain normal fault growth by relieving gravitational forcing
- Surface processes enable a wide range of fault life spans in thick faulted layer

Supporting Information:
- Readme
- Figure S1
- Table S1
- Text S1

Correspondence to:
J.-A. Olive,
jaolive@mit.edu

Citation:
Olive, J.-A., M. D. Behn, and L. C. Malatesta (2014), Modes of extensional faulting controlled by surface processes, *Geophys. Res. Lett.*, *41*, 6725–6733, doi:10.1002/2014GL061507.

Received 12 AUG 2014
Accepted 22 SEP 2014
Accepted article online 26 SEP 2014
Published online 9 OCT 2014

Modes of extensional faulting controlled by surface processes

Jean-Arthur Olive[1], Mark D. Behn[2], and Luca C. Malatesta[3]

[1]Massachusetts Institute of Technology/Woods Hole Oceanographic Institution Joint Program in Oceanography, Cambridge, Massachusetts, USA, [2]Department of Geology and Geophysics, Woods Hole Oceanographic Institution, Woods Hole, Massachusetts, USA, [3]Division of Geological and Planetary Sciences, California Institute of Technology, Pasadena, California, USA

Abstract We investigate the feedbacks between surface processes and tectonics in an extensional setting by coupling a 2-D geodynamical model with a landscape evolution law. Focusing on the evolution of a single normal fault, we show that surface processes significantly enhance the amount of horizontal extension a fault can accommodate before being abandoned in favor of a new fault. In simulations with very slow erosion rates, a 15 km thick brittle layer extends via a succession of crosscutting short-lived faults (heave <5 km). By contrast, when erosion rates are comparable to the regional extension velocity, deformation is accommodated on long-lived faults (heave >10 km). Using simple scaling arguments, we quantify the effect of surface mass removal on the force balance acting on a growing normal fault. This leads us to propose that the major range-bounding normal faults observed in many continental rifts owe their large offsets to erosional and depositional processes.

1. Introduction

Erosion, sediment transport, and deposition can strongly affect the state of stress and deformation at plate boundaries through the redistribution of surficial masses. These processes are well documented and have been extensively modeled in active orogens [e.g., *Koons*, 1989; *Molnar and England*, 1990; *Avouac and Burov*, 1996; *Willett*, 1999], where surface processes affect the balance of tectonic forces at the scale of the orogenic wedge. Specifically, it has been established that active surface processes favor strain localization along a few long-lived thrusts and back thrusts that are active synkinematically, thereby promoting sustained exhumation of deep crustal units [e.g., *Mugnier et al.,* 1997; *Willett*, 1999; *Konstantinovskaia and Malavieille*, 2005]. By contrast, the morphology of extensional environments is largely controlled by the geometry of a succession of lithospheric-scale normal faults that accommodate most of the strain near the axis of the rift. Potential feedbacks between surface processes and extensional tectonics should therefore be investigated in terms of a force balance at the scale of these individual faults. This study presents a simple mechanical framework quantifying the effect of surface processes on fault geometry and longevity, which is currently lacking in extensional settings.

Earlier studies of the long-term (0.1–10 Myr) coupling between erosion and rifting largely focused on the plate boundary scale and investigated complex feedbacks between surface processes and viscous flow in a multilayered lithosphere. *Burov and Cloething* [1997] and *Burov and Poliakov* [2001] showed that erosion of the rift shoulder and sedimentation in the rift neck lead to greater lithospheric thinning and basin widening by affecting lithospheric strength profiles. More recently, *Bialas and Buck* [2009] used numerical models to argue that enhanced sedimentation in the northern Gulf of California promotes a transition to narrow rifting compared to the wider, more distributed rifting in the south. They attributed this result to sediments decreasing the change in gravitational force caused by the growth of topography during extension, thereby promoting prolonged extension in a narrow region. Unfortunately, due to their large-scale approach, their models did not properly resolve individual normal faults and therefore could not test how changes in gravitational force affected the behavior of a specific normal fault.

Indeed, a key parameter in the evolution of extensional plate boundaries is the amount of offset that can be accommodated by a single normal fault before being abandoned in favor of a new one. Broadly speaking, fault life span determines whether the "building block" of a rift system is a half-graben structure (characteristic offset smaller than the faulted layer thickness, typically a few kilometers), a long-lived, low-angle detachment fault (with offset in the 10–50 km range, resulting in surficial exposure of lower crustal units), or a combination of

both [e.g., *Morley*, 1995; *Lavier et al.,* 2000; *Lavier and Buck*, 2002; *Whitney et al.,* 2012]. Over the past two decades, a robust conceptual framework has been assembled to identify the first-order controls on the modes of extensional faulting [e.g., *Forsyth*, 1992; *Buck*, 1993; *Lavier et al.,* 2000; *Lavier and Buck*, 2002; *Behn and Ito*, 2008; *Olive and Behn*, 2014]. These authors considered the mechanical cost of sustaining slip on a single normal fault, which requires an increase in tensional force as extension proceeds. The necessary force increase was shown to be faster in thicker elastoplastic-faulted layers. Consequently, the force threshold for breaking a new fault is met sooner in thicker layers, and extension proceeds by a succession of short-lived normal faults. If the faulted layer is sufficiently thin, the force buildup is moderate and the threshold may never be reached, favoring a succession of large offset faults.

A major limitation of this theory is that for brittle layer thicknesses typical of most continental rift zones, only small offset faults are predicted, yet faulting in these regions range from short-lived faults to long-lived detachments forming metamorphic core complexes [e.g., *Whitney et al.,* 2012]. Additional controls such as rapid hydrothermal cooling [*Lavier and Buck*, 2002] and magmatic processes [*Buck et al.,* 2005] have been proposed to explain large offset faulting, but those are more relevant to mid-ocean ridge settings and thus cannot explain this discrepancy between the models and observations in continental rifts. On the other hand, subaerial rifts are subjected to surface processes that rework topography more or less efficiently depending on climatic parameters and basement lithology. By redistributing mass at the surface, these processes have the potential to modify the stress state of the lithosphere and thus influence fault evolution.

The aim of the present study is to quantify the effect of surface processes on fault life span in an extensional regime. To do so, we conduct 2-D geodynamic simulations of fault evolution coupled to a parameterized erosion and deposition model. We complement this numerical approach with a force balance model that explicitly considers the gravitational contribution of topography, a term that was previously parameterized only in combination with footwall and hanging wall flexure [e.g., *Forsyth*, 1992; *Buck*, 1993] or ignored [*Olive and Behn*, 2014]. We find that when acting at rates comparable to fault slip, surface processes can significantly enhance fault life span by relieving a fraction of the topographic forcing. We identify faulting regimes controlled by the efficiency of surface processes and faulted layer thickness and discuss their applicability to natural rift systems.

2. Numerical Experiments

We solve for conservation of mass, momentum, and energy in a 2-D domain using the finite difference/marker-in-cell technique [*Harlow and Welch*, 1965] described by *Gerya* [2010]. Our model setup (Figure 1a) is similar to that of *Olive and Behn* [2014] and treats the brittle upper crust as an elastoplastic layer of thickness H, Young's modulus E (100 GPa), and Poisson's ratio ν (0.5). The brittle layer lies above a weak viscous lower crust (Newtonian, with viscosity 10^{18} Pa s), and beneath a low-viscosity "sticky air" layer (viscosity 10^{17} Pa s) [*Crameri et al.,* 2012]. The base of the faulted layer corresponds to the 600°C isotherm and evolves with temperature. Thermal conductivity is artificially enhanced such that thermal diffusion occurs faster than fault-induced advection, thereby allowing the faulted layer to retain its initial thickness during fault growth [*Lavier and Buck*, 2002]. This allows us to isolate the effect of redistributing surficial mass from that of advective thinning of the brittle layer.

The air layer has a density of 10^{-2} kg m^{-3}; the brittle and lower crustal layers have densities of 2700 kg m^{-3}. To insure that deformation is not influenced by the model boundaries, the width of the box is set to 3 times the (elastic) flexural wavelength of the brittle layer. We pull on each side of the domain at a half rate, V, and compensate the horizontal outflow of air and rock by imposing a matching inflow of material through the top and bottom boundaries of the numerical domain, respectively. Shear tractions are set to zero on all boundaries.

Localized plastic failure (i.e., faulting) occurs spontaneously in our simulations following a Drucker-Prager criterion that approximates an inscribed Mohr-Coulomb yield surface with a friction coefficient of 0.6. Strain localization is promoted by decreasing the material cohesion (initially $C_0 = 100$ MPa) linearly with accumulated plastic strain [*Lavier et al.,* 2000] down to a value of 0.01 MPa after a critical plastic strain corresponding to ~200 m of fault offset has been exceeded. To initialize strain localization on a single normal fault, we impose a

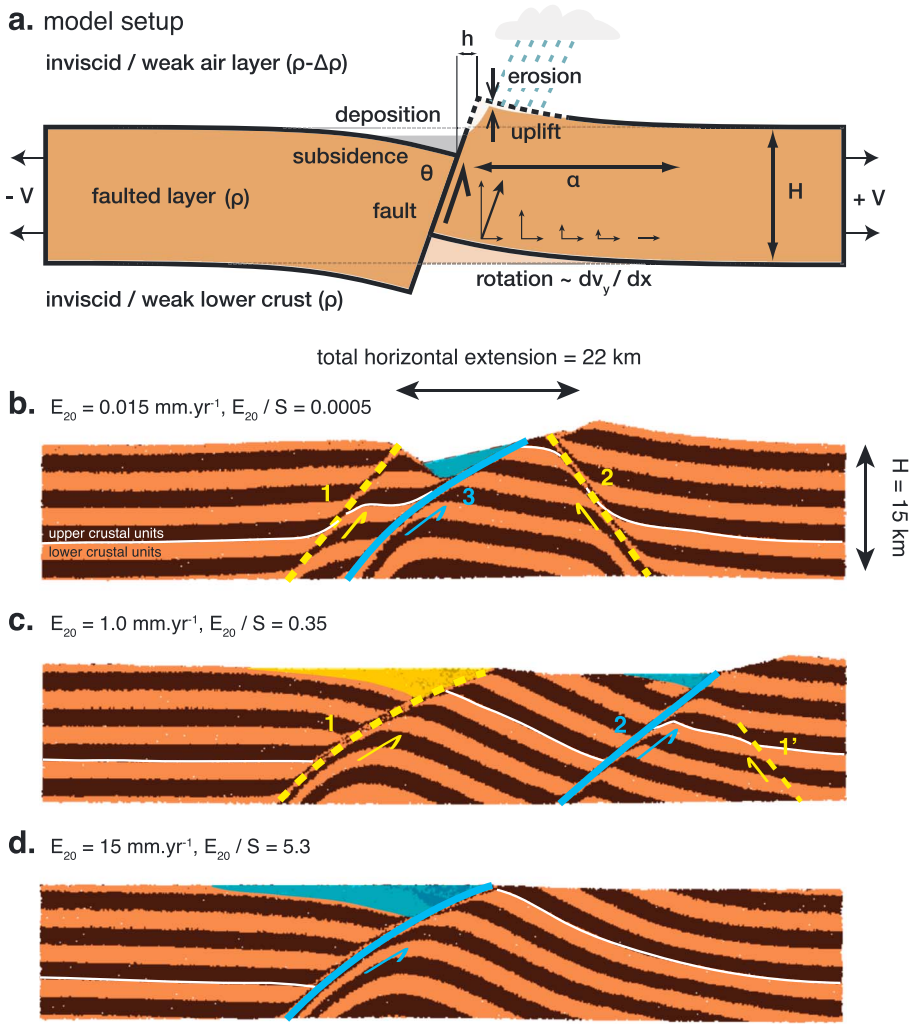

Figure 1. (a) Setup of the numerical and force balance model. An elastoplastic layer of thickness *H* with a weak fault initially seeded at a $\theta = 60°$ angle undergoes extension at a half-rate *V*. The layer has density ρ and is sandwiched between two weak/inviscid layers (not shown). As the fault accumulates horizontal offset *h*, the hanging wall and footwall blocks undergo flexure (over a wavelength α), which results in topography growth and fault rotation. The material upwelling beneath the footwall has the same lithology as the brittle layer but acquires its brittle nature through thermal equilibration as it cools below 600°C. Surface processes cause footwall erosion and partial filling of flexural basins. Snapshots of numerical simulations after 22 km of extension in a 15 km thick layer extending at a half rate of 1 mm yr^{-1}. Surface topography is subjected to erosion rates (calibrated on a 20° mean elevation slope) of (b) 0.015, (c) 1.0, and (d) 15 mm yr^{-1}. Yellow dashed lines indicate faults that have been abandoned in a sequence indicated by the numbers. Blue faults are actively growing at the time of the snapshot. Colored areas indicate the material that deposited while the fault of corresponding color was active. In the case of Figure 1b, where faults are short-lived and closely spaced, the blue material integrates deposits associated with the successive growth of faults #2 and #3. The solid white line marks the top of lower crustal units.

rectangular "fault seed" of dip $\theta_0 = 60°$ and width equal to about two grid cells in the middle of the domain within the brittle layer at the beginning of each model run. In this narrow region, plastic strain is set to the critical value and cohesion is decreased accordingly. A "healing" mechanism is implemented to promote strain localization [*Poliakov and Buck*, 1998].

Surface topography, *y(x)*, is tracked using a chain of closely spaced markers that separate the air layer from the brittle rock layer. At the end of each "tectonic" time step (Δt), the topography is advected using the current velocity field. We then modify the topography by solving a landscape evolution law on the surface marker chain over the time Δt. All markers located above the updated topography become of type "air" (i.e., acquire the density and rheological properties of the weak air layer), while markers located beneath become "rock." This new marker distribution is then used to calculate the next "tectonic" velocity field.

The first step in our landscape evolution model consists of eroding topography to create a surface that reflects the mean elevation profile of a mountain range. The 2-D nature of our approach simplifies the average of the profiles of concave-up trunk rivers and convex-up ridgelines to a largely constant slope that relaxes to shallower angles across the foothills. To do so, we scale the erosion rate with the local slope:

$$\frac{\partial y}{\partial t} = -K\left|\frac{\partial y}{\partial x}\right|^n \quad (1)$$

Because the profile of mean elevations differs from that of the trunk river, we omit the upstream drainage area component used in stream power models [e.g., *Whipple*, 2004, and references therein]. We set $n = 1.3$, which was empirically found to generate realistic topographies across a range of K values. The coefficient K accounts for erosional resistance and climatic conditions and can be calibrated at field sites where mean elevation slope and erosion rate are known. For simplicity, we hereafter refer to various values of K (the main control on the efficiency of surface processes) in terms of the corresponding erosion rate in a 20° sloping mountain front, E_{20}, defined as

$$E_{20} = K\tan^n(20°) \quad (2)$$

Following the erosion step, we identify watersheds across the model domain by first locating the topographic highs. We calculate the volume of eroded material in each watershed and then deposit that volume horizontally at the bottom of the same watershed. The flat deposition at the toe of the slopes simulates sediment redistribution processes in floodplains or playas. Deposition ceases if the eroded volume exceeds the current basin capacity. In this scenario, the filled basin is then integrated with the neighboring watershed at the next erosion step. Negligible sedimentation occurs in watersheds that border the model domain because the edges of the model act as sinks allowing the material to leave the domain.

We conducted 21 numerical simulations in which we systematically varied E_{20} between 0.015 and 150 mm yr^{-1}, with an emphasis on the geologically relevant interval of 0.015–10 mm yr^{-1} [e.g., *Herman et al.*, 2013]. We chose a brittle layer thickness of 15 km extending at a half rate of either 1 or 10 mm yr^{-1}, which is representative of many continental rifts [e.g., *Chen and Molnar*, 1983; *Strak*, 2012]. We also examined cases with a 25 km thick layer, representing colder rifts such as certain portions of the East African Rift or the Baikal Rift [*Lavier and Buck*, 2002]. A summary of our simulation parameters is given in the supporting information. In each run, we measure the total amount of horizontal extension (h_{MAX}) accommodated on the initial fault when (if) the next fault breaks; or more precisely when accumulated plastic strain starts to heal on the initial fault and build up on the new fault. We also monitor the progressive rotation of the initial fault and characterize the modes of faulting (e.g., multiple, short-lived faults versus a single long-lived detachment) over ~40 km of total extension.

3. Results

In all numerical simulations, shear deformation localizes rapidly along the seeded fault, inducing flexural uplift and subsidence of the footwall and hanging wall blocks, respectively (Figure 1a). The exposed fault scarp systematically features the steepest slopes and is therefore subjected to the fastest erosion. The corresponding erosion products deposit in the flexural basin formed by the subsiding hanging wall, while the ridge of the footwall retreats away from the basin. As extension proceeds on the fault, an equilibrium topography consisting of a footwall high and a partially filled hanging wall basin is reached in cases where E_{20} and V are of the same order of magnitude. Topography is essentially suppressed when E_{20} exceeds ~5 times the extension half-rate V.

Our numerical simulations reveal that for a given layer thickness and extension rate, increasing the erosion rate E_{20} can have a dramatic effect on the modes of faulting. Figures 1b–1d shows snapshots of layer deformation after 22 km of total extension in a 15 km thick layer at a half-rate $V = 1$ mm yr^{-1}. At very low erosion rates ($E_{20} = 0.015$ mm yr^{-1}, Figure 1b), the initial fault accommodates ~3.7 km of extension before an antithetic fault breaks and takes up the next ~6 km of extension, uplifting and subsequently eroding the sediments deposited in the hanging wall of the first fault. A third antithetic fault then forms, and new sediments begin infilling the basin formed by the third active fault and the topographic high inherited, but not yet eroded, from the second fault. Extension therefore proceeds as a succession of short-offset antithetic faults.

By contrast, at a higher erosion rate of 1 mm yr^{-1}, the initial fault remains active longer and accommodates more extension. In this case, the first ~10 km of extension are taken up on the initial fault, followed by the development of two blind antithetic faults in the footwall block. Over the next few kilometers of extension, the two small faults (1′ and 2 in Figure 1c) accommodate a significant fraction of the total plate separation, until the fault dipping parallel to the master fault cuts through the entire layer and localizes all the extension (Fault 2 in Figure 1c), resulting in abandonment of the initial master fault. Fault 2 becomes the next master fault, and the same pattern repeats. Extension is therefore taken up by a succession of large offset (10–15 km) subparallel faults. A topographic high can only be sustained in the footwall of the actively growing fault since erosion rapidly levels the topography once a fault is abandoned.

Finally, at very high erosion rates ($E_{20} = 15$ mm yr^{-1}) (Figure 1d), the initial fault remains active indefinitely, accommodating ≥ 50 km of extension (corresponding to the extent of the simulation). Significant flexural deformation occurs in the footwall, and lower crustal units become exposed at the surface. However, no characteristic topography can develop as the (unrealistically) high erosion rates force the surface to remain flat throughout the experiment.

Figure 2a (and Table S1 in the supporting information) shows the life span h_{MAX} of the initially seeded fault plotted against the reference erosion rate E_{20} normalized by the average fault slip rate S. Faults in a 15 km thick brittle layer subjected to slow erosion rates ($E_{20} \leq 0.15$ mm yr^{-1}) accommodate ~4 km of extension before being abandoned, regardless of extension rate. Fault life span is weakly sensitive to very slow erosion rates, but increases sharply when the ratio of erosion rate to long-term fault slip rate E_{20}/S exceeds ~0.1. $E_{20}/S >$ ~2 promote infinite growth of the initial normal fault and the suppression of all topography. Brittle layer thickness strongly modulates the sensitivity of fault life span to surface processes. Consistently with earlier studies, fault life span is systematically shorter in a 25 km thick layer than in a 15 km thick layer, across the entire range of E_{20}/S (Figure 2a). Moreover, while extremely fast normalized erosion rates ($E_{20}/S >$ ~2) lead to infinite fault growth in a 15 km thick layer, these rates only extend fault life span to 15 km in a 25 km thick lithosphere.

In addition to topography and fault life span, we also monitor the evolving fault dip by visually fitting a line to the region of greatest accumulated plastic strain (Figure 2b). When fault offset becomes comparable to the thickness of the faulted layer, the fault develops significant concave down curvature [e.g., *Choi and Buck*, 2012]. In these situations, we restrict our visual fit to the upper half of the faulted layer to yield an upper estimate of fault rotation. Faults rotate rapidly from their initial angle (~60°) down to dips of 30–45°, in accordance with a model in which the fault rotates to minimize the total extensional work [*Olive and Behn*, 2014]. We find that fault rotation is slower in a 25 km thick faulted layer than in a 15 km thick layer, consistent with the predictions of *Olive and Behn* [2014]. Rotation progressively slows with total extension, reaching a minimum dip when the total fault heave exceeds the faulted layer thickness. The amount of rotation at a given time depends solely on the faulted layer thickness and the amount of extension accommodated on the fault. Thus, surface processes act to prolong fault life span but do not strongly influence the kinematics of fault rotation.

4. Topographic Forcing on Fault Life Span

To further quantify the influence of surface processes on fault life span, we complement our numerical approach with a simple force balance model for a growing normal fault [*Buck*, 1991; *Lavier et al.,* 2000; *Behn and Ito*, 2008]. The basic assumption of this class of models is that an active fault will be abandoned when the force required to keep it active exceeds the threshold force needed to break a new fault. The total force, F, represents the depth-averaged deviatoric stress acting on the fault [*Forsyth*, 1992] and can be decomposed into the force required to sustain frictional slip on the fault, F_{FRIC}, the force required to bend the footwall and hanging wall blocks as the fault accumulates offset, F_{BEND}, and the force required to sustain topography, F_{TOPO}.

By definition, the work done by the bending and topographic forces corresponds to the internal strain energy stored in the faulted layer and to the change in gravitational potential energy associated with topography buildup, respectively. F_{BEND} and F_{TOPO} can therefore be expressed as the derivative of those work terms with respect to horizontal extension [*Forsyth*, 1992; *Buck*, 1993; *Olive and Behn*, 2014]. We estimate these forces by

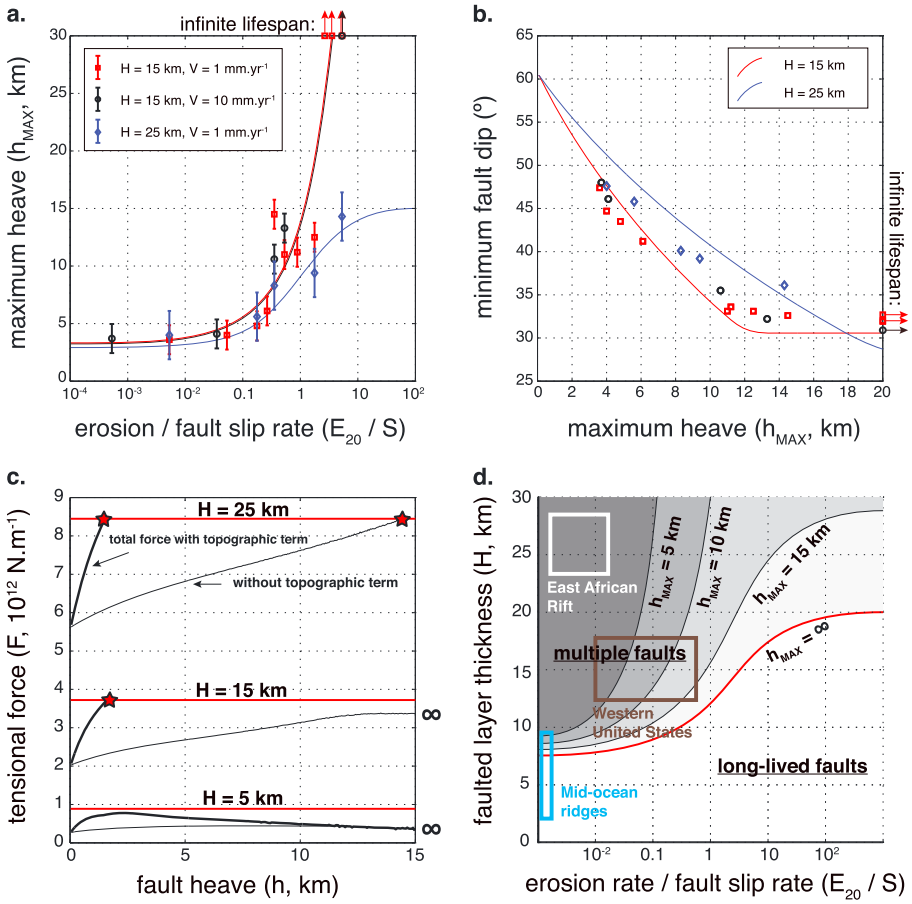

Figure 2. (a) Maximum heave accommodated on the initial normal fault in the numerical model, as a function of erosion rate (E_{20}, calibrated on 20° mean elevation slopes) normalized by the long-term fault slip rate ($S = 2\,V/\cos\,\theta$, assuming a mean fault dip of 45°). Data points span various brittle layer thicknesses and extension rates (see legend). Arrows indicate cases where faults grew indefinitely. The error bars correspond to three cell sizes near the fault (~1.5 km), which sets the uncertainty in our measurement of fault life span. The red, black, and blue curves illustrate the behavior expected from our force balance model, with the color key indicated in the legend. (b) Lowest dip reached by the initial normal fault (initially dipping 60°) when it becomes abandoned in favor of a new fault (or for an "infinite" amount of offset). The red and blue curves correspond to our kinematic model of fault rotation (see supporting information) in a 15 km and a 25 km thick faulted layer, respectively. (c) Force needed to sustain slip on a normal fault as a function of accumulated heave, for various faulted layer thicknesses *H*. The thick and thin lines show the total force with and without the component corresponding to topography growth F_{TOPO}, respectively. The red stars mark the amount of horizontal extension that can be accommodated when the force threshold to break a new fault in intact lithosphere (horizontal red line) is reached. The infinity symbols indicate cases where faults can grow indefinitely. (d) Conceptual regime diagram showing fault life span h_{MAX} as a function of faulted layer thickness and the ratio of erosion rate to long-term slip rates, as inferred from our force balance model. Representative parameter values are indicated for various extensional settings.

treating the faulted layer as an elastoplastic thin plate [*Buck,* 1988, 1993] with a triangular yield strength envelope approximating that used in the numerical simulations. Fault topography, after a given amount of horizontal extension *h*, is modeled as the flexural readjustment to the rigid uplift/subsidence of the footwall and hanging wall [*Weissel and Karner*, 1989; *Olive and Behn*, 2014]. Plate rigidity is decreased iteratively in regions of high plate curvature, until the effective elastic bending moment matches that of the elastoplastic plate [*Buck*, 1988]. The flexure equation with spatially varying rigidity is then solved with finite difference to obtain the fault-induced topography *y(x)*. The bending work W_{BEND} is obtained by integrating the bending stress times the bending strain over the entire layer. The topographic work corresponds to the change in gravitational potential energy associated with offsetting the air-rock density contrast, $\Delta\rho$, from its initial flat state.

It has long been recognized that fault dip plays a key role in modulating the forces acting on a fault [*Forsyth*, 1992]. Here we incorporate fault rotation to the force balance model using a simple kinematic approach.

Following *Olive and Behn* [2014], we assume that fault rotation results from passive advection of the fault in the displacement field induced by the flexure of the footwall and hanging wall blocks. The rotational component of this displacement field is due largely to the decreasing magnitude of vertical motion that occurs over approximately one flexural wavelength from the fault (Figure 1a). The average rotation rate therefore inversely scales with the flexural wavelength and is slower in stronger, thicker layers.

Once the modeled fault topography is obtained for a given amount of extension h, we infer the effective flexural wavelength of our elastoplastic thin plate and use it to update the fault angle at step $h + \Delta h$ (see details in the supporting information). To prevent the fault from reaching very low dip angles in the force balance model, which are not observed in the numerical models, we assume that rotation ceases once the heave becomes comparable to the faulted layer thickness. This corresponds to faults that have acquired significant curvature after footwall rollover has occurred [*Choi and Buck*, 2012]. This approach is simpler to implement in an elastoplastic layer than the energy minimization model of *Olive and Behn* [2014] and predicts similar rotation kinematics, suggesting that flexural rotation allows faults to stay close to their lowest energy configuration (see supporting information). Our predictions of fault rotation are shown in Figure 2b and match the results of our numerical simulations. In particular, slower rotation in the thicker 25 km layer is well explained by the scaling of rotation rates with the inverse of flexural wavelength ($\sim H^{3/4}$).

Armed with a self-consistent force balance model that incorporates fault rotation, we can now quantify the effect of topographic growth on fault life span. In Figure 2c we plot the increase in the total force acting on a growing fault with and without the topographic component F_{TOPO} (thick and thin black lines, respectively). Ignoring F_{TOPO} in the force balance is analogous to cases in which erosion and deposition rapidly suppress topographic growth, i.e., $E_{20} \gg S$ in our numerical simulations. Consistent with *Buck* [1993] and *Lavier et al.* [2000], we find that faults growing in thin layers ($H < \sim 10$ km) remain active indefinitely as the force required to sustain fault slip never exceeds the threshold to break a new fault. This occurs regardless of the incorporation of F_{TOPO}. By contrast, thicker ($\geq$10 km) layers only produce small offset (~2 km) faults when F_{TOPO} is included in the force balance. However, removing F_{TOPO} (as would correspond to more rapid erosion and deposition rates) causes a dramatic increase in fault life span. In particular, for layer thicknesses of 15–25 km, removing F_{TOPO} has a significantly greater effect on fault life span than does brittle layer thickness. Finally, we note that the topographic force accounts for a smaller proportion of the total force acting on a fault when the brittle layer is thicker. This explains why very active surface processes promote infinite fault growth in 15 km thick layers, while only extending fault life span to ~15 km in 25 km thick layers.

5. Application to Rift Systems

The conceptual regime diagram shown in Figure 2d summarizes our findings. This is analogous to the regime diagrams proposed by *Lavier et al.* [2000] and *Lavier and Buck* [2002] with a new parameter accounting for the efficiency of surface processes at relieving topographic loads. Continental rifts are frequently characterized by a brittle layer thickness of ~15 km, as inferred from seismicity, flexural, and heat flow constraints [*Chen and Molnar*, 1983]. Models that do not include surface processes predict that faulting in a 15 km thick brittle layer (i.e., the upper continental crust) should proceed by a succession (or synkinematic slip) of moderate-offset ($h_{MAX} \sim 3$–5 km) normal faults leading to the formation of grabens and half grabens. However, significant offset has been observed along major faults of the Basin and Range province. For instance, the Wasatch fault in Utah has accumulated as much as 11 km of vertical offset [*Parry and Bruhn*, 1987]. As shown above, such large offsets in 15–25 km thick lithosphere can only occur if surface processes relieve a portion of the topographic forcing, provided that erosion acts at rates comparable to tectonic slip. Thermochronologic studies suggest long-term slip rates on the Wasatch fault of ~0.4 mm.yr^{-1} over the last ~10 Myrs [*Naeser et al.,* 1983] and erosion rates ranging from 0.07 to 0.14 mm.yr^{-1} in Wasatch Mountains river catchments along the Weber segment [*Stock et al.,* 2009]. These erosion rates can be extrapolated to a representative E_{20} value of ~0.16 mm.yr^{-1} after calibration against local mean elevation slopes. This yields a ratio of $E_{20}/S \sim 0.4$, which in our models promotes fault life span as large as 10–15 km. Thus, we propose that the Wasatch fault owes its significant life span to the coupling between tectonics and surface processes. Further, by ensuring a longer fault life span, surface processes promote further rotation away from a steep Andersonian initiation angle and indeed dips as low as ~30–45° have been proposed for the Wasatch fault [*Harris et al.,* 2000].

Some rift zones (e.g., the Baikal Rift, portions of the East African Rift and the Gulf of Suez) are associated with thicker brittle layers (25–30 km) potentially inherited from a cratonic lithosphere and/or associated with lower heat flow [e.g., *Chen and Molnar*, 1983; *Lavier and Buck*, 2002]. Along the East-African Rift, for instance, many half-grabens feature valley-bounding faults that accommodate only a few kilometers of extension before deformation jumps to another locus [e.g., *Morley*, 1995] and large-offset normal faults are absent. This is consistent with the slow erosion rates (<0.1 mm.yr^{-1}) inferred over the East African Rift [*Herman et al.,* 2013]. However, active glacial erosion may have locally contributed to anomalously high displacement (>6 km) on horst-bounding faults, as proposed in the Rwenzori Mountains [*Ring*, 2008].

Finally, we note that mid-ocean ridges are generally characterized by thin (<10 km) lithosphere and very limited erosion and sedimentation. Thus, fault evolution and the frequency of large-offset oceanic detachment faults in these environments are likely controlled by the thin lithosphere and the kinematic effects of dike emplacement [*Buck et al.,* 2005; *Tucholke et al.,* 2008]. However, *Choi and Buck* [2012] showed that volcanic infill of flexural basins can influence patterns of fault evolution at ridges, and thus even in these environments, surface mass redistribution may play a role in controlling the mode of faulting.

6. Conclusions

In conclusion, we have shown that surface processes can significantly enhance the life span of an individual normal fault, provided they act on a time scale comparable to, or faster than, long-term tectonic rates. We suggest that erosion and deposition are essential in sustaining slip on large-offset range bounding normal faults at continental rifts which would otherwise have been abandoned after a few kilometers of offset. Future challenges include the following: (1) parameterizing the effects of erosion in a way that can be linked to climatic parameters [e.g., *Willett*, 2009] and (2) investigating the three-dimensional feedbacks between fault growth and surface processes, which may include controls on fault segmentation and linkage.

Acknowledgments
The authors wish to thank Don Forsyth, Brian Yanites, and Eric Mittelstaedt as well as Taylor Perron and his group for fruitful discussions. This work was supported by NSF grants OCE-1154238 and EAR-1010432. Input files and scripts used for the numerical simulations are available upon request by emailing the corresponding author at jaolive@mit.edu.

The Editor thanks Phaedra Upton and one anonymous reviewer for their assistance in evaluating this paper.

References

Avouac, J.-P., and E. B. Burov (1996), Erosion as a driving mechanism of intracontinental mountain growth, *J. Geophys. Res.*, *101*, 17,747–17,769, doi:10.1029/96JB01344.

Behn, M. D., and G. Ito (2008), Magmatic and tectonic extension at mid-ocean ridges: 1. Controls on fault characteristics, *Geochem. Geophys. Geosyst.*, *9*, Q08O10, doi:10.1029/2008GC001965.

Bialas, R. W., and W. R. Buck (2009), How sediment promotes narrow rifting: Application to the Gulf of California, *Tectonics*, *28*, TC4014, doi:10.1029/2008TC002394.

Buck, W. R. (1988), Flexural rotation of normal faults, *Tectonics*, *7*, 959–973, doi:10.1029/TC007i005p00959.

Buck, W. R. (1991), Modes of continental extension, *J. Geophys. Res.*, *96*, 20,161–20,178, doi:10.1029/91JB01485.

Buck, W. R. (1993), Effect of lithospheric thickness on the formation of high- and low-angle normal faults, *Geology*, *21*(10), 933–936, doi:10.1130/0091-7613(1993)021<0933:EOLTOT>2.3.CO;2.

Buck, W. R., L. L. Lavier, and A. N. B. Poliakov (2005), Modes of faulting at mid-ocean ridges, *Nature*, *434*, 719–723.

Burov, E. B., and S. Cloething (1997), Erosion and rift dynamics: New thermomechanical aspects of post-rift evolution of extensional basins, *Earth Planet. Sci. Lett.*, *150*, 7–26.

Burov, E. B., and A. N. B. Poliakov (2001), Erosion and rheology controls on synrift and postrift evolution: Verifying old and new ideas using a fully coupled numerical model, *J. Geophys. Res.*, *106*, 16,461–16,481, doi:10.1029/2001JB000433.

Chen, W.-P., and P. Molnar (1983), Focal depths of intracontinental and intraplate earthquakes and their implications for the thermal and mechanical properties of the lithosphere, *J. Geophys. Res.*, *88*, 4183–4214, doi:10.1029/JB088iB05p04183.

Choi, E., and W. R. Buck (2012), Constraints on the strength of faults from the geometry of rider blocks in continental and oceanic core complexes, *J. Geophys. Res.*, *117*, B04410, doi:10.1029/2011JB008741.

Crameri, F., H. Schmeling, G. J. Golabek, T. Duretz, R. Orendt, S. J. H. Buiter, D. A. May, B. J. P. Kaus, T. V. Gerya, and P. J. Tackley (2012), A comparison of numerical surface topography calculations in geodynamic modelling: An evaluation of the 'sticky air' method, *Geophys. J. Int.*, *189*, 38–54, doi:10.1111/j.1365-246X.2012.05388.x.

Forsyth, D. W. (1992), Finite extension and low-angle normal faulting, *Geology*, *20*(1), 27–30, doi:10.1130/0091-7613(1992)020<0027:FEALAN>2.3.CO;2.

Gerya, T. (2010), *Introduction to Numerical Geodynamic Modelling*, Cambridge Univ. Press, Cambridge, U. K.

Harlow, F. H., and J. E. Welch (1965), Numerical calculation of time-dependent viscous incompressible flow of fluid with free surface, *Phys. Fluids*, *8*(12), 2182–2189, doi:10.1063/1.1761178.

Harris, R. A., R. B. Smith, W. L. Chang, C. Meertens, and A. Friedrich (2000), Temporal distribution of extensional strain across the southern Wasatch fault zone—Geological constraints for the GPS velocity field, *Eos Trans. AGU*, *81*, 1230.

Herman, F., D. Seward, P. G. Valla, A. Carter, B. Kohn, S. D. Willett, and T. A. Ehlers (2013), Worldwide acceleration of mountain erosion under a cooling climate, *Nature*, *504*, 423–426, doi:10.1038/nature12877.

Konstantinovskaia, E., and J. Malavieille (2005), Erosion and exhumation in accretionary orogens: Experimental and geological approaches, *Geochem. Geophys. Geosyst.*, *6*, Q02006, doi:10.1029/2004GC000794.

Koons, P. O. (1989), The topographic evolution of collisional mountain belts—A numerical look at the Southern Alps, New Zealand, *Am. J. Sci.*, *289*, 1041–1069.

Lavier, L. L., and W. R. Buck (2002), Half graben versus large-offset low-angle normal fault: Importance of keeping cool during normal faulting, *J. Geophys. Res.*, *107*(B6), 2122, doi:10.1029/2001JB000513.

Lavier, L. L., W. R. Buck, and A. N. B. Poliakov (2000), Factors controlling normal fault offset in an ideal brittle layer, *J. Geophys. Res.*, *105*, 23,431–23,442, doi:10.1029/2000JB900108.

Molnar, P., and P. England (1990), Late Cenozoic uplift of mountain ranges and global climate change: Chicken or egg?, *Nature*, *346*, 29–34.

Morley, C. K. (1995), Developments in the structural geology of rifts over the last decade and their impact on hydrocarbon exploration, in *Hydrocarbon Habitat in Rift Basins*, *Geol. Soc. London Spec. Publ.*, *80*, 1–32, doi:10.1144/GSL.SP.1995.080.01.01.

Mugnier, J. L., P. Baby, P. Colletta, P. Vinous, P. Balé, and P. Leturmy (1997), Thrust geometry controlled by erosion and sedimentation: A view from analogue models, *Geology*, *25*, 427–430.

Naeser, C. W., B. Bryant, M. D. J. Crittenden, and M. L. Sorensen (1983), Fission-track ages of apatite in the Wasatch Mountains, Utah: An uplift study, in *Tectonics and Stratigraphy of the Eastern Great Basin*, edited by D. M. Miller et al., *Mem. Geol. Soc. Am.*, *157*, 29–36.

Olive, J.-A., and M. D. Behn (2014), Rapid rotation of normal faults due to flexural stresses: An explanation for the global distribution of normal fault dips, *J. Geophys. Res. Solid Earth*, *119*, 3722–3739, doi:10.1002/2013JB010512.

Parry, W. T., and R. L. Bruhn (1987), Fluid inclusion evidence for minimum 11 km vertical offset on the Wasatch fault, Utah, *Geology*, *15*, 67–70, doi:10.1130/0091-7613(1987)15<67:FIEFMK>2.0.CO;2.

Poliakov, A. N. B., and W. R. Buck (1998), Mechanics of stretching elastic-plastic-viscous layers: Applications to slow-spreading mid-ocean ridges, in *Faulting and Magmatism at Mid-Ocean Ridges*, *Geophys. Monogr. Ser.*, vol. 106, edited by W. R. Buck et al., pp. 305–323, AGU, Washington, D. C.

Ring, U. (2008), Extreme uplift of the Rwenzori Mountains in the East African Rift, Uganda: Structural framework and possible role of glaciations, *Tectonics*, *27*, TC4018, doi:10.1029/2007TC002176.

Stock, G. M., K. L. Frankel, T. A. Ehlers, M. Scheller, S. M. Briggs, and R. C. Finkel (2009), Spatial and temporal variations in denudation of the Wasatch Mountains, Utah, USA, *Lithosphere*, *1*(1), 34–40, doi:10.1130/L15.1.

Strak, V. (2012), L'évolution du relief le long des escarpements de faille normale active: Observations, modélisations expérimentales et numériques, PhD thesis, Univ. Pierre et Marie Curie, Paris, France.

Tucholke, B. E., M. D. Behn, W. R. Buck, and J. Lin (2008), Role of melt supply in oceanic detachment faulting and formation of megamullions, *Geology*, *36*, 455–458.

Weissel, J. K., and G. D. Karner (1989), Flexural uplift of rift flanks due to mechanical unloading of the lithosphere during extension, *J. Geophys. Res.*, *94*, 13,919–13,950, doi:10.1029/JB094iB10p13919.

Whipple, K. X. (2004), Bedrock rivers and the geomorphology of active orogens, *Annu. Rev. Earth Planet. Sci.*, *32*, 151–185, doi:10.1146/annurev.earth.32.101802.120356.

Whitney, D. L., C. Teyssier, P. Rey, and W. R. Buck (2012), Continental and oceanic core complexes, *Geol. Soc. Am. Bull.*, doi:10.1130/B30754.1.

Willett, S. D. (1999), Orogeny and orography: The effects of erosion on the structure of mountain belts, *J. Geophys. Res.*, *104*, 28,957–28,981, doi:10.1029/1999JB900248.

Willett, S. D. (2009), Erosion on a line, *Tectonophysics*, *484*, 168–180, doi:10.1016/j.tecto.2009.09.011.